Journal of Thermal Science Vol.30, No.4 (2021) 1421−1434

https://doi.org/10.1007/s11630-021-1483-7 **Article ID: 1003-2169(2021)04-1421-14**

Efficient Modeling of an Axial Compressor with Swirl Distortion

GUO Jin*, HU Jun, WANG Xuegao, TU Baofeng

College of Energy and Power Engineering, Nanjing University of Aeronautics and Astronautics, Jiangsu Province Key Laboratory of Aerospace Power Systems, Nanjing 210016, China

Abstract: This paper presents a satisfactory numerical strategy to reliably evaluate the three-dimensional large-scale flow feature of multistage axial compressors in response to complex swirl distortion with acceptable computational cost. Under the theoretical framework of the body force method, the guide vanes of a swirl distortion generator and the multiple blade rows of a two-stage low-speed axial compressor are described by distributed source terms instead of a complex body-fitted grid approach. The key flow structure of the paired swirl generated by the swirl generator and the main distributions of flow angle at the rotor outlet of the first stage captured by the model agree well with experimental results, demonstrating the effectiveness of the numerical strategy. Additionally, the interaction process between the steady-state paired swirl and the compressor is clearly revealed by the study. The intensity of the swirl distortion can be greatly reduced after passing through the axial compressor. However, the swirl has a significant impact on the local blade loading of the first stage, which induces the mass flux nonuniformity as well as total pressure and total temperature distortion. The combined total pressure and total temperature distortion is significantly attenuated near tip and slightly enhanced near hub as it moves through the second stage.

Keywords: axial compressor, vane-based, paired swirl, source terms, numerical simulation

1. Introduction

The problem of inlet-engine compatibility has been one of the hot issues of research related to aero gas turbine engines. Swirl distortion is becoming increasingly important in the investigations on this problem with the development of modern aircraft propulsion systems. Numerous factors can cause swirl distortion, such as serpentine inlet ducts, cross winds, and ground vortices. To this end, the Society of Automotive Engineers (SAE) S-16 Turbine Engine Inlet Flow Distortion Committee has published a guideline for addressing steady-state swirl distortion [1]. In the guideline, swirl distortion is subdivided into the following four categories: (1) bulk swirl, (2) tightly-wound vortices, (3) paired swirl, and (4) cross-flow swirl. Among them, bulk swirl and paired swirl are the most common types of swirl distortion.

There have been studies highlighting the generation methods of swirl distortion during direct-connect tests for compressors and engines. Gressler et al. earlier investigated the use of turned vanes and delta wings to produce certain strength of bulk swirl and paired swirl [2]. Sheoran and Bouldin proposed a flexible and adaptable swirl distortion generator based on the swirl chamber concept [3, 4]. Moreover, they created a

Received: Jan 05, 2020 AE: DU Juan Corresponding author: GUO Jin E-mail: guojin_nj@126.com

Nomenclature

E, F, G	inviscid fluxes	t	time/s
E_v, F_v, G_v	viscid fluxes	π	circular constant
r, θ, z	radial, circumferential and axial coordinate/m	**Subscripts**	
S	Centrifugal and Coriolis source terms	r, θ, z	radial, circumferential and axial direction
S_b	blockage source terms	**Superscript**	
S_F	blade force source terms	T	transposition

widely-recognized set of swirl distortion descriptors, including swirl intensity (SI), swirl directivity (SD) and swirl pairs (SP) [5]. Based on the concept of vane-based generators, Hoopes and O'Brein established a novel approach to generate swirl distortion [6]. The approach is named as the StreamVane method. Unlike the previous methods for generating generic swirl patterns, the method can reproduce an arbitrary swirl profile. Guimarães et al. measured flow details from the StreamVane distortion generator with particle image velocimetry [7]. They took an in-depth look at turbulence structure and aerodynamic scaling of the mean flow in the generated swirl distortion. Frohnapfel et al. carried out experimental studies of fan rotor effects on inlet swirl generated by the StreamVane device, and their investigations revealed that small-scale features of the distortion were less affected by the fan rotor while large-scale ones were nearly eliminated [8]. More recently, Dong et al. experimentally investigated the effectiveness of casing treatments on a low-speed single-stage compressor with swirl distortion which was generated by a set of plane guide vanes [9]. Overall, a common method of generating swirl distortion in experiments is arranging a certain number of guide vanes with a specific layout in a hollow pipe.

In addition, considerable research efforts have been devoted to the effects of swirl distortion on compression system of engines. Pardo et al. [10] investigated the effects of tightly-wound vortices on the performance of a transonic compressor, using frozen rotor models. Yao [11] and Fidalgo et al. [12] utilized full-annuals unsteady Reynolds-averaged Navier-Stokes (RANS) simulations to investigate total pressure distortion transfer in compressors. The results showed that pressure-induced swirl plays an important role in the physical process of the distortion transfer across blade rows. Assuredly, high-fidelity Computational Fluid Dynamics (CFD) simulations provide in-depth understanding of flow mechanisms occurring in the interaction between complex swirl distortion and compressors. Nevertheless, given the current computational resources, there is a contradiction between high-fidelity simulations and fast simulations. At this stage, the high computational costs required for the high-fidelity CFD simulations make this kind of method unacceptable for the industrial department to evaluate the tolerance of multistage compressors to inlet distortion.

In practice, designers pay more attention to the large-scale characteristics of complex inlet distortion transfer in multistage compressors in the initial phase of compressor design. Some research has been conducted over the years to develop appropriate numerical strategies that can quantify the large-scale features of complex swirl distortion in multistage compressors with the affordable computational costs. Cousins and Davis introduced some extensions to the classical parallel compressor model to perform the simulation of complex distortion including swirl distortion in compressors [13, 14]. However, the effects of radial distortion cannot be predicted with the theory of parallel compressor model in essence. Complex swirl flow is often distorted along the circumferential and radial directions, which is more difficult to treat.

In recent decades, the technical concept of three-dimensional (3-D) body force model has attracted more interest. This kind of model focuses on the flow phenomenon that the scale is much larger than the blade pitch. The flow in each blade passage of turbomachinery is averaged along the circumferential direction, and blade force source terms are introduced to replace the effect of blade surface. Previous studies have demonstrated the ability of this model to simulate compressor response to large-scale total pressure distortion [15–18]. However, limited effort has been devoted to extend and assess the ability of the 3-D body force model to predict the effect of complex swirl distortion, which requires a more complete consideration of the correlation between the blade force and the inlet flow direction.

Additionally, the numerical strategy for the vane-based swirl distortion generators is also significant for predicting the compressor response to the designative swirl pattern. Ordinarily, swirl generator geometry modeling and complex meshing generation are challenging and time-consuming for regular CFD simulations. In reality, immersed boundary method has mathematically shown that the effect of any solid wall immersed in fluid can be strictly equivalent to distributed force sources [19]. Therefore, the aforementioned body force model can be regarded as a simplified method of

dimensionality reduction in turbomachinery flow by the immersed boundary method. Inspired by the idea of the immersed boundary method, an efficient mathematical model is proposed to model vane-based swirl distortion generators without detailed gridding of vanes in this paper. To evaluate the applicability of a previously-developed 3-D body force model [20] to complex swirl distortion problem, the developed mathematical model is further integrated into the 3-D body force model to simulate the flow process of a steady-state large-scale paired swirl distortion in a two-stage low-speed axial compressor. Comparisons of computed and experimental results are presented to support the effectiveness of the aforementioned models.

In the following sections, we first make a brief introduction to the test rig of the investigated compressor for swirl distortion. Subsequently, the efficient mathematical model for the vane-based swirl distortion generator is established. The theoretical frame of the previously-developed 3-D body force model is reorganized and enriched for highlighting the correlation between the blade force and the inlet flow direction. Finally, the numerical simulation of the flow behavior in the compressor with the paired swirl distortion is performed. Discussions are presented to give further insight into the interaction process between the steady-state swirl distortion and the multistage compressor.

2. Compressor Test Rig for Swirl Distortion

2.1 Test rig

A schematic view of the test rig is shown in Fig. 1. The test rig mainly consists of a vane-based swirl distortion generator and a low-speed axial compressor. The research compressor has two stages without any inlet guide vanes. The main design parameters are summarized in Table 1.

The swirl distortion generator integrated in the test rig can produce different kinds of swirl distortion by installing vanes in a certain layout. In this investigation, a large-scale steady-state paired swirl is generated by two sets of vanes with opposite stagger angle. Fig. 2 shows the layout of guide vanes in the swirl distortion generator. A set of straight vanes with positive stagger angle of 20° labeled as A1–A5 are utilized to produce co-swirl. Another set of straight vanes with negative stagger angle of 20° labeled as B1–B5 are used to generate counter-swirl. The circumferential interval between the vanes in the same group is 22.5°. The two sets of vanes share same design parameters, as detailed in Table 2.

2.2 Experiment measurement

In order to provide sufficient data for verifying the reliability of the models, the flow characteristic of compressor at 800 r/min is tested. Particularly, the flow parameters on the sections A and B of the compressor shown in Fig. 3(a) are measured in detail. The schematic of the experimental measurement is shown in Fig. 3(b). The section A is located about double diameter of the pipe downstream the swirl distortion generator to obtain the basically stable flow field formed by the upstream swirl distortion generator. The section B is the outlet of the first-stage rotor of the compressor.

The distributions of the flow parameters at different circumferential points along the radial direction are measuring via radial displacement mechanisms and five-hole probes. In the section A, 12 radial displacement mechanisms are arranged along the circumferential direction to drive 12 L-shaped five-hole probes. In view of the complicated spatial distribution characteristics of the flow field of the swirl distortion, the swirl distortion generator shown in Fig. 3(b) is driven by a stepping motor and the transmission structure of worm geared and rotated along the circumferential direction to precisely measure the distribution of flow parameters. The corresponding spatial locations of the swirl distortion

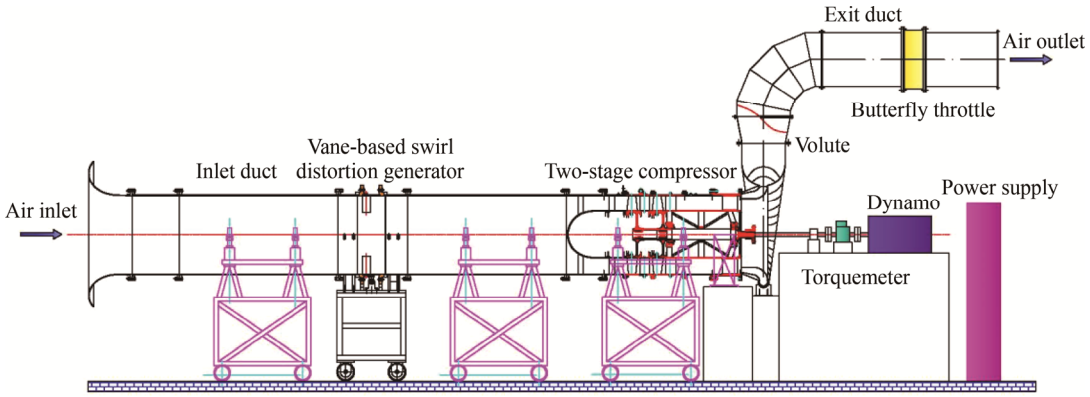

Fig. 1 Schematic drawing of compressor test rig for swirl distortion

Table 1 Design parameters of the compressor

Parameter	Design value
Wheel speed/r·min^{-1}	1500
Outside diameter/mm	900
Mass flow/kg·s^{-1}	25
Total pressure ratio	1.035
Number of rotor blades (R1/R2)	19/22
Number of stator blades (S1/S2)	18/20
Hub-to-tip ratio	0.6
Tip clearance of the first-stage rotor/mm	1.5
Tip clearance of the second-stage rotor/mm	1.2
Blade type	NACA-65-010

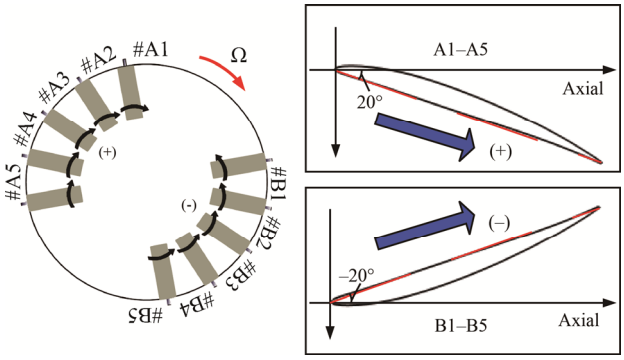

Fig. 2 Layout of guide vanes in swirl distortion generator for paired swirl

generator and the five-hole probes are changed to measure the flow parameters in more circumferential points. In the specific measurement, the flow parameters at 20 radial points are measured by the five-hole probe combined with the radial displacement mechanism. The minimum measuring radius of the inner ring is 75 mm and the maximum measuring radius of the outer ring is 445 mm. At each radial position, the swirl distortion generator rotates 6° each time and 5 times in total. Hence, 60 measuring points in a whole circumferential ring can be obtained. The measuring method of the section B is similar to that of the section A. The four-hole probe, instead of the five-hole probe, is applied to adapt to the small rotor-stator axial distance. The section B has 10 radial and 60 circumferential measuring points, respectively. To enlarge the measuring range and improve the accuracy, the pre-deflection angle is set when the probe is installed in the section B.

Table 2 Design parameters of the vanes in the swirl distortion generator

Parameter	Design value
Vane height/mm	200
Vane chord length/mm	100
Vane bending angle/(°)	20
Inlet metal angle/(°)	10
Vane type	NACA 65

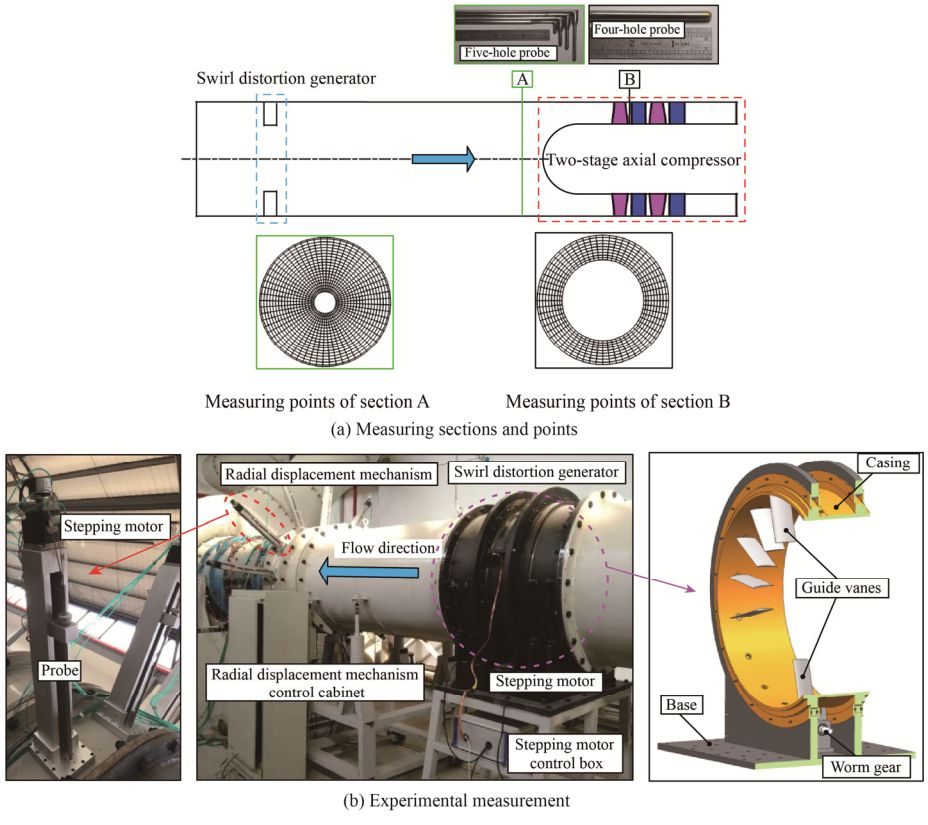

Fig. 3 Experimental rig of two-stage low speed axial flow compressor for swirl distortion

3. Numerical Methodology

3.1 Vane-based swirl distortion generator

It is still a challenging and time-consuming task to mesh the vane-based swirl distortion generator by using the conventional CFD method. Inspired by the immersed boundary method [19], the present study transforms the guide vanes of swirl distortion generator into distributed source terms in the flow equations, which avoids the generation of complex mesh of the vane geometry.

The grid of the computational domain constructed for the swirl distortion generator is plotted in Fig. 4. The main control equation adopted by the model is as follows.

$$\frac{\partial \boldsymbol{U}}{\partial t}+\frac{\partial\left(\boldsymbol{E}-\boldsymbol{E}_{\mathrm{v}}\right)}{\partial z}+\frac{1}{r}\frac{\partial\left(\boldsymbol{F}-\boldsymbol{F}_{\mathrm{v}}\right)}{\partial \theta}+\frac{1}{r}\frac{\partial r\left(\boldsymbol{G}-\boldsymbol{G}_{\mathrm{v}}\right)}{\partial r}=\boldsymbol{S}+\boldsymbol{S}_{\boldsymbol{F}} \tag{1}$$

where

$$\begin{cases}\boldsymbol{U}=\left[\rho \quad \rho v_z \quad \rho v_\theta \quad \rho v_r \quad \rho e\right]^{\mathrm{T}}\\ \boldsymbol{E}=\left[\rho v_z \quad \rho v_z^2+p \quad \rho v_\theta v_z \quad \rho v_r v_z \quad v_z\left(\rho e+p\right)\right]^{\mathrm{T}}\\ \boldsymbol{F}=\left[\rho v_\theta \quad \rho v_z v_\theta \quad \rho v_\theta^2+p \quad \rho v_r v_\theta \quad v_\theta\left(\rho e+p\right)\right]^{\mathrm{T}}\\ \boldsymbol{G}=\left[\rho v_r \quad \rho v_z v_r \quad \rho v_\theta v_r \quad \rho v_r^2+p \quad v_r\left(\rho e+p\right)\right]^{\mathrm{T}}\\ \boldsymbol{E}_{\mathrm{v}}=\left[0 \quad \tau_{zz} \quad \tau_{z\theta} \quad \tau_{zr} \quad \tau_{zz}v_z+\tau_{z\theta}v_\theta+\tau_{zr}v_r-q_z\right]^{\mathrm{T}}\\ \boldsymbol{F}_{\mathrm{v}}=\left[0 \quad \tau_{\theta z} \quad \tau_{\theta\theta} \quad \tau_{\theta r} \quad \tau_{\theta z}v_z+\tau_{\theta\theta}v_\theta+\tau_{\theta r}v_r-q_\theta\right]^{\mathrm{T}}\\ \boldsymbol{G}_{\mathrm{v}}=\left[0 \quad \tau_{rz} \quad \tau_{r\theta} \quad \tau_{rr} \quad \tau_{rz}v_z+\tau_{r\theta}v_\theta+\tau_{rr}v_r-q_r\right]^{\mathrm{T}}\\ \boldsymbol{S}=\left[0 \quad 0 \quad \frac{-\rho v_\theta v_r+\tau_{r\theta}}{r} \quad \frac{\rho v_\theta^2+p-\tau_{\theta\theta}}{r} \quad 0\right]^{\mathrm{T}}\\ \boldsymbol{S}_{\boldsymbol{F}}=\left[0 \quad F_z \quad F_\theta \quad F_r \quad 0\right]^{\mathrm{T}}\end{cases} \tag{2}$$

where ρ is the density; v is the flow velocity; p is the static pressure; F is the blade force of per unit volume of airflow; τ is the turbulent viscous stress; q is the turbulent heat flux, and e is the total energy of per unit mass of airflow. The term e is defined as

$$e=\frac{p}{\rho\left(\gamma-1\right)}+\frac{1}{2}\left(v_z^2+v_\theta^2+v_r^2\right) \tag{3}$$

where γ is the specific heat ratio.

The turbulent stress and heat conduction are solved based on the eddy viscosity hypothesis proposed by Boussinesq. By analogy with the viscous flow law of the laminar flow, the corresponding eddy viscosity coefficient μ_{t}, turbulent thermal diffusivity k_{t}, and turbulent Prandtl number Pr_{t} are defined to correlate turbulent effect with mean flow. The specific expression is shown in Eq. (4).

$$\begin{cases}\tau_{zz}=\mu_{\mathrm{t}}\left(2\frac{\partial v_z}{\partial z}-\frac{2}{3}\nabla\cdot\vec{v}\right)\\ \tau_{\theta\theta}=\mu_{\mathrm{t}}\left(2\left(\frac{\partial v_\theta}{r\partial\theta}+\frac{v_r}{r}\right)-\frac{2}{3}\nabla\cdot\vec{v}\right)\\ \tau_{rr}=\mu_{\mathrm{t}}\left(2\frac{\partial v_r}{\partial r}-\frac{2}{3}\nabla\cdot\vec{v}\right)\\ \tau_{z\theta}=\tau_{\theta z}=\mu_{\mathrm{t}}\left(\frac{\partial v_\theta}{\partial z}+\frac{\partial v_z}{r\partial\theta}\right)\\ \tau_{zr}=\tau_{rz}=\mu_{\mathrm{t}}\left(\frac{\partial v_r}{\partial z}+\frac{\partial v_z}{\partial r}\right)\\ \tau_{r\theta}=\tau_{\theta r}=\mu_{\mathrm{t}}\left(\frac{\partial v_\theta}{\partial r}+\frac{\partial v_r}{r\partial\theta}-\frac{v_\theta}{r}\right)\\ q_z=-k_{\mathrm{t}}\frac{\partial T}{\partial z}\quad q_\theta=-k_{\mathrm{t}}\frac{\partial T}{r\partial\theta}\quad q_r=-k_{\mathrm{t}}\left(\frac{\partial rT}{r\partial r}-\frac{T}{r}\right)\\ k_{\mathrm{t}}=\frac{c_p\mu_{\mathrm{t}}}{Pr_{\mathrm{t}}}\end{cases} \tag{4}$$

where c_p is the specific heat ratio of constant pressure and T is the static temperature.

The source term $\boldsymbol{S}_{\boldsymbol{F}}$, only applied in the blue region in Fig. 4, is employed instead of the geometry of the guide vanes to simulate the turning effect of two sets of vanes on the flow in the swirl distortion generator. Similar to Marble's analysis [21], the source terms are divided into two parts: one is inviscid part, which is perpendicular to the flow direction and responsible for flow turning; and the other is viscid part, which represents the viscous effect of vanes. For the straight vane, the radial force of vane F_r can be ignored, and only the circumferential force F_θ and axial force F_z are simulated. Additionally, due to the limited flow loss formed by the swirl distortion generator, the viscous effect of the vanes is ignored. The terms F_θ and F_z are carried out by Eqs. (5)–(6).

$$F_\theta^{n+1}=F_\theta^n+C\left(v_\theta^{\mathrm{target}}-v_\theta\right) \tag{5}$$

$$F_z=-F_\theta\frac{v_\theta}{v_z} \tag{6}$$

where n and n+1 represents the adjacent time intervals. The term C is the artificial iteration constant to adjust the stability and convergence speed of calculation.

As can be found in Eq. (5), the circumferential velocity of the flow field will be consistent with the input target circumferential velocity $v_\theta^{\mathrm{target}}$ when the calculation reaches to the final convergence. The velocity $v_\theta^{\mathrm{target}}$ is determined by Eq. (7).

$$v_\theta^{\mathrm{target}}=v_z\tan\left(\kappa+\delta\right) \tag{7}$$

where κ and δ are the geometric angle and deviation angle of the blade, respectively. The initial value of δ can be estimated by the Carters' rule [22] and further

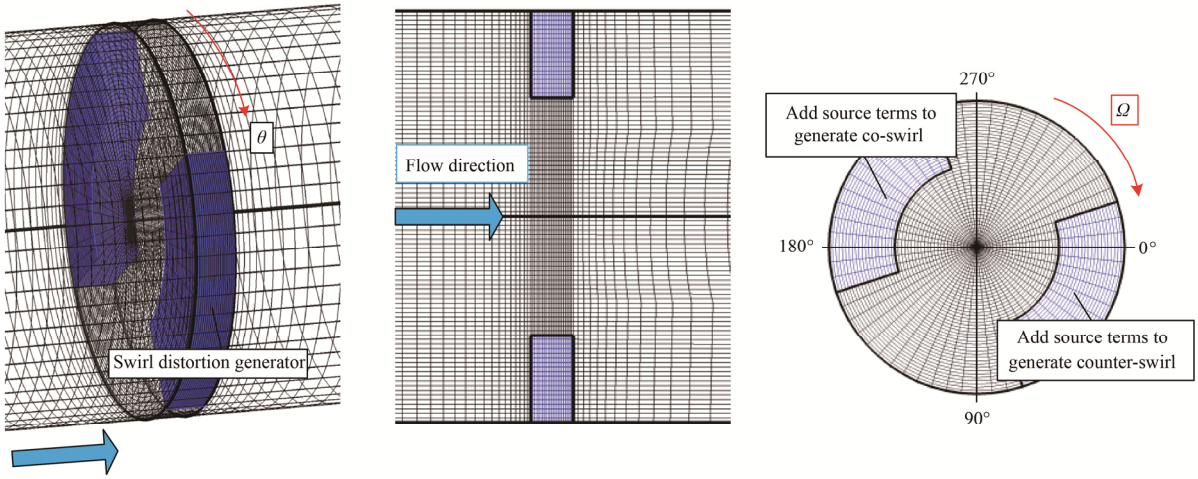

(a) 3-D view (b) Meridian view (c) Circumferential view

Fig. 4 Computational mesh of vane swirl distortion generator

modified by the experimental data to obtain the appropriate swirl distortion intensity.

3.2 Multiple blade rows of compressor

Guo and Hu [20] recently proposed a 3-D body force model to investigate the response of multistage axial-flow compressor to inlet total pressure distortion. The present paper further evaluates the applicability of the model to complex swirl distortion. The computational mesh of the two-stage compressor is shown in Fig. 5.

The governing equations in the rotor/stator region of the two-stage compressor are as follows:

$$\left(\frac{\partial}{\partial t}+\Omega\frac{\partial}{\partial\theta}\right)b\boldsymbol{U}+\frac{\partial b\left(\boldsymbol{E}-\boldsymbol{E}_{\mathrm{v}}\right)}{\partial z}+\frac{1}{r}\frac{\partial rb\left(\boldsymbol{G}-\boldsymbol{G}_{\mathrm{v}}\right)}{\partial r} = b\boldsymbol{S}+\boldsymbol{S}_b+b\boldsymbol{S}_F \tag{8}$$

where

$$\begin{cases}\boldsymbol{S}_b=\left[0 \quad p\dfrac{\partial b}{\partial z} \quad 0 \quad p\dfrac{\partial b}{\partial r} \quad 0\right]^{\mathrm{T}}\\ \boldsymbol{S}_F=\left[0 \quad F_z \quad F_\theta \quad F_r \quad F_\theta\Omega r\right]^{\mathrm{T}}\end{cases} \tag{9}$$

where b is the blade blockage coefficient to reflect the influence of the blade finite thickness and defined as:

$$b=N\left|\theta_p-\theta_s\right|/2\pi \tag{10}$$

where N is the number of blades, and π is circular constant. The terms θ_p and θ_s are the circumferential coordinate system of the pressure surface and suction surface of the blade, respectively.

The common assumption of such models [17, 18] is that the flow in the rotor passages is locally axisymmetric in the relative coordinate system and the flow in the stator passages is locally axisymmetric in the absolute coordinate system. The term $\Omega\partial/\partial\theta$ is introduced when the time term of the rotor region is transformed from the relative coordinate system to the absolute coordinate system. The detail derivation is given in Ref. [17]. When there exits circumferential distortion in the inlet flow, it can represent the side flow effect caused by the blade rotation observed in the absolute coordinate system of the rotor passages while the blade rotation angular velocity Ω in the stator passages is taken as 0.

The distributed body force in $\boldsymbol{S_F}$ is utilized to replace the effect of blade geometry on the flow. The unknown term can be written as

$$\boldsymbol{F}_b=\left[F_z \quad F_\theta \quad F_r\right]^{\mathrm{T}} \tag{11}$$

The term is the blade force source term. The core modeling method is to associate the source term with the local flow state to realize the response of the source term to the upstream inlet disturbance.

The blade force is divided into the inviscid force φ and viscous force f. The viscous force, reverse and parallel to the direction of relative velocity w, is mainly for simulating the flow loss caused by the blade boundary layer.

$$\begin{bmatrix}f_z\\ f_\theta\\ f_r\end{bmatrix}=-\frac{f}{w}\begin{bmatrix}v_z\\ v_\theta-\Omega r\\ v_r\end{bmatrix} \tag{12}$$

The local viscous force f is calculated by the loss coefficient ϖ in the basic flow passage.

$$\begin{cases}f=\rho T\dfrac{v_{\mathrm{m}}}{w}\dfrac{\Delta s}{\Delta m}\\ \Delta s=-R\ln\left[1-\dfrac{\varpi\left(1-\left(1+\dfrac{\gamma-1}{2}Ma_{\mathrm{r},1}^2\right)^{-\frac{\gamma}{\gamma-1}}\right)}{\left(T_{\mathrm{r},2}^*/T_{\mathrm{r},1}^*\right)^{\frac{\gamma}{\gamma-1}}}\right]\end{cases} \tag{13}$$

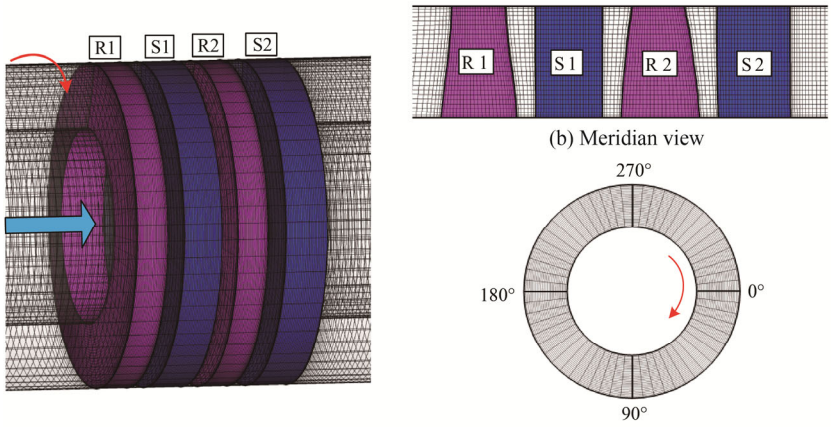

Fig. 5 Computational mesh of two-stage low speed axial compressor

where w is the relative velocity; v_{m} is the meridional velocity; Δs is the entropy increase in the basic passage; Δm is the length of the basic meridional passage; R is the gas constant, and $Ma_{\mathrm{r},1}$ is the relative Mach number at the inlet of the rotor passages. The terms $T^*_{\mathrm{r},1}$ and $T^*_{\mathrm{r},2}$ represent the relative total temperature at the inlet and outlet of the rotor passages, respectively. The terms $Ma_{\mathrm{r},1}$, $T^*_{\mathrm{r},1}$, and $T^*_{\mathrm{r},2}$ become absolute parameters for the stator passages.

The inviscid force, perpendicular to the relative flow direction, is applied to control the flow direction.

$$\varphi_z v_z + \varphi_\theta \left(v_\theta - \Omega r\right) + \varphi_r v_r = 0 \tag{14}$$

The circumferential component of the inviscid force φ_θ is obtained from the steady-state circumferential momentum equation of the target circumferential velocity $v_\theta^{\mathrm{target}}$. The radial inviscid force is associated with the mean cambered surface in the 3-D blade, as presented in Eq. (15).

$$\begin{cases} \varphi_\theta = F_\theta - f_\theta = \dfrac{1}{b}\dfrac{\partial b\left(\rho v_z v_\theta^{\mathrm{target}} - \tau_{z\theta}\right)}{\partial z} \\ \qquad + \dfrac{1}{br}\dfrac{\partial rb\left(\rho v_\theta^{\mathrm{target}} v_r - \tau_{r\theta}\right)}{\partial r} \\ \qquad - \left(\dfrac{-\rho v_\theta^{\mathrm{target}} v_r}{r} + \dfrac{\tau_{r\theta}}{r}\right) \\ \left(v_\theta^{\mathrm{target}}\right)_{\mathrm{rotor}} = \Omega r - v_{\mathrm{m}} \tan\left(\kappa + \delta\right) \\ \left(v_\theta^{\mathrm{target}}\right)_{\mathrm{stator}} = v_{\mathrm{m}} \tan\left(\kappa + \delta\right) \\ \varphi_r = \dfrac{\varphi_\theta n_r}{n_\theta} \end{cases} \tag{15}$$

where n_r and n_θ are the normal vectors of middle cambered surface in the blade along the radial and circumferential direction, respectively. Thus, the blade forces in three dimensions can be determined by combining Eqs. (12)–(15) when the deviation angle δ and loss coefficient ϖ of the blade are known.

A large tangential velocity is at the inlet of the blade passage when there exits the swirl flow. This may lead to changes in the inlet velocity triangles and then affect the incidence and Mach number at the inlet of the blade passage, as shown in Fig. 6. Following the throughflow theory of turbomachines, the model relates the blade characteristics, the deviation angle and loss coefficient, to the incidence and inlet Mach number, which fully represents the effect of the inlet swirl flow on the distribution of blade loading. The deviation angle and loss coefficient are divided into several parts, as given in Eq. (16).

$$\begin{cases} \delta = \delta_{\mathrm{ref}} + \delta_{\mathrm{off}} + \delta_{\mathrm{3D}} \\ \varpi = \varpi_{\mathrm{ref}} + \varpi_{\mathrm{off}} + \varpi_{\mathrm{3D}} \end{cases} \tag{16}$$

The terms δ_{ref} and ϖ_{ref} are the reference part corresponding to the reference incidence. The determination of these parameters mainly refers to the correlation of Lieblein [23]. The terms δ_{3D} and ϖ_{3D}, based on the models developed by Roberts [24], Lakshminarayana [25], Howell [26], and Banjac [27], are utilized for simulating the influence of tip clearance and secondary flow. The terms δ_{off} and ϖ_{off} are the non-reference parts and determined by the method of Creveling [27]:

$$\begin{cases} \dfrac{\delta_{\mathrm{off}}}{i_{\mathrm{ref}} + \kappa_{\mathrm{i}} - \left(\delta_{\mathrm{ref}} + \kappa_{\mathrm{o}}\right)} = f\left[\dfrac{i - i_{\mathrm{ref}}}{i_{\mathrm{ref}} + \kappa_{\mathrm{i}} - \left(\delta_{\mathrm{ref}} + \kappa_{\mathrm{o}}\right)}\right] \\ \dfrac{\varpi_{\mathrm{off}}}{\left(i - i_{\mathrm{ref}}\right)^2} = f\left(Ma, h\right) \end{cases} \tag{17}$$

In particular, the source term of blade force not only depends on the deviation angle and loss coefficient but also is closely coupled with the local instantaneous flow parameters. The effect of the 3-D geometry of the blade

is fully considered. Hence, the 3-D nonlinear characteristics of the distorted flow in the compressor can be well reflected.

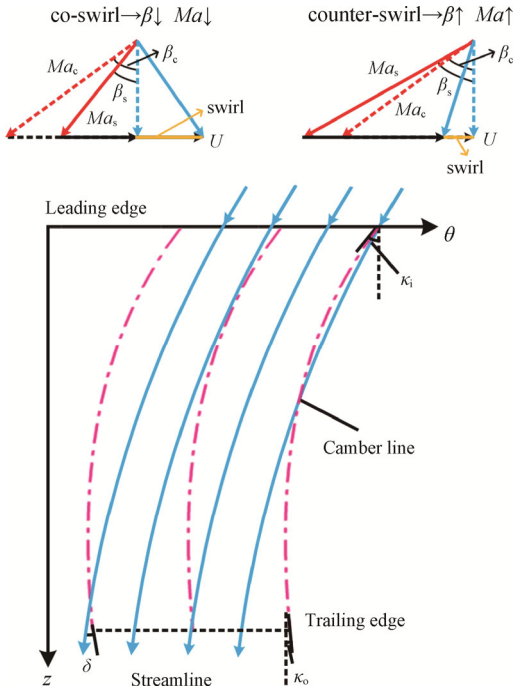

Fig. 6 Inlet velocity triangle of blade passage with swirl

It needs to be emphasized again that both the mathematical model for the swirl distortion generator and the body force model for multistage compressors are based on the basic idea of immersion boundary method to some extent. Comparatively, the blade force modeling method of the swirl distortion generator is more general but introduces the coefficient requiring artificial adjustment. Whereas the local dimension reduction is carried out in the 3-D body force model for the axisymmetric layout of the turbomachinery.

3.3 Discrete method for governing equations

The element centered finite volume method is applied to discretize the control equations of the foregoing models. The time term is explicitly promoted by the four-step Runge-Kutta method [28]. This method enables to eliminate the high-frequency errors and improve the stability of the calculation. For the steady calculation, the local time step Δt can be taken as the adjacent time step to further accelerate the convergence of the flow solution. The low-diffusion flux-splitting scheme (LDFSS) [29] proposed by Edwards is employed to deal with the inviscid flux. The monotone upstream-centered scheme for conservation laws (MUSCL) [30] and minmod limiter are utilized to achieve the guaranteed monotony and second-order accuracy. The LDFSS divides the inviscid flux into the convective flux term and pressure flux term for solution respectively, which has high resolution of shock wave and contact discontinuity.

The viscous fluxes are determined by the eddy viscosity coefficient μ_t, turbulent thermal diffusivity k_t, and partial derivatives of the related flow parameters. The model focuses on the characteristics of the large-scale flow in the main flow region but not on the small-scale viscous flow in the near wall region. The wall boundary of the hub and shroud is treated as an inviscid slip boundary to avoid solving the small-scale viscous flow in the near wall region and further accelerate the calculation. The eddy viscosity coefficient μ_t is carried out by a simple semi empirical method proposed by Gallimore [31]. The value of the criterion number $\mu_t/\rho v_z L_{ref}$ is pre-determined in the flow field. The term L_{ref} is the characteristic length of the compressor. The local value of μ_t is then obtained according to the local instantaneous flow parameters. The turbulent Prandtl number Pr_t in the flow field is set to 0.9 in advance and combines with the local value of μ_t to gain the local turbulent thermal diffusivity k_t.

4. Results and Discussion

4.1 Flow downstream of vane-based swirl generator

A set of swirl indexes proposed by Bouldin and Shearan [5] are adopted to conduct comprehensive quantitative analysis for the steady-state swirl distortion upstream of the compressor. The swirl indexes include the swirl intensity index SI, swirl direction index SD, and swirl pair index SP, as follows:

$$\mathrm{SI}=\frac{\int_{\theta^+}\alpha(\theta)\mathrm{d}\theta+\left|\int_{\theta^-}\alpha(\theta)\mathrm{d}\theta\right|}{360^\circ} \tag{18}$$

$$\mathrm{SD}=\frac{\int_{\theta^+}\alpha(\theta)\mathrm{d}\theta+\int_{\theta^-}\alpha(\theta)\mathrm{d}\theta}{\int_{\theta^+}\alpha(\theta)\mathrm{d}\theta+\left|\int_{\theta^-}\alpha(\theta)\mathrm{d}\theta\right|} \tag{19}$$

$$\mathrm{SP}=\frac{\int_{\theta^+}\alpha(\theta)\mathrm{d}\theta+\left|\int_{\theta^-}\alpha(\theta)\mathrm{d}\theta\right|}{2\times\max\left[\int_{\theta^+}\alpha(\theta)\mathrm{d}\theta,\left|\int_{\theta^-}\alpha(\theta)\mathrm{d}\theta\right|\right]} \tag{20}$$

where $\alpha(\theta)$ is the circumferential distribution of the absolute flow angle at equal radius. The definitions of θ^+ and θ^- are illustrated in Fig. 7.

Fig. 8 displays a comparison of the contours of the absolute circumferential flow angle on the section A obtained by the model and experimental result. Fig. 9 plots the quantitative comparisons of the radial distributions of SI, SD, and SP between the calculated and the experimental results. As can be found from these comparisons, the numerical method based on the source term can quickly and reasonably reproduce the twin swirl generated by the swirl distortion generator in the experimental conditions. It also can be seen from Fig. 9,

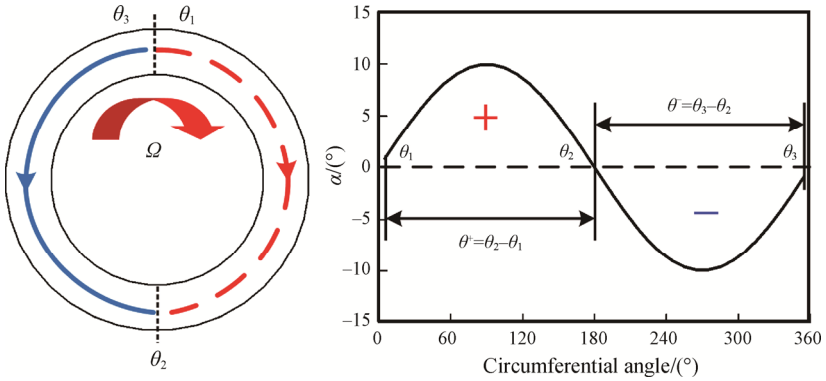

Fig. 7 Typical distribution of the absolute flow angle at equal radius

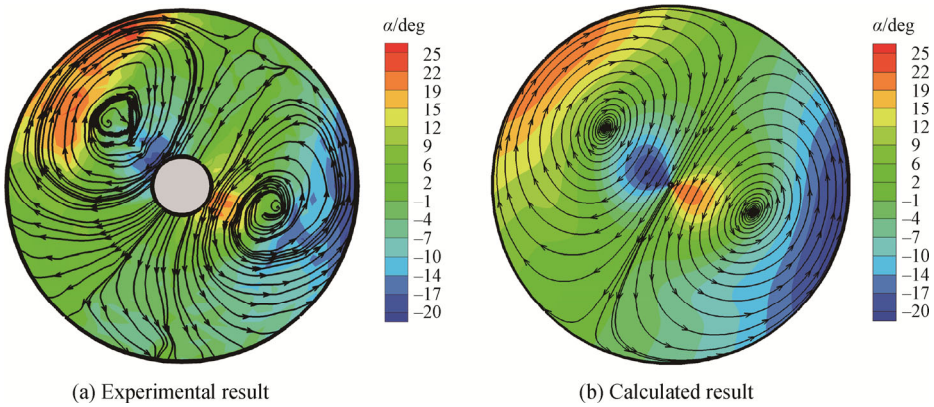

Fig. 8 Contours of absolute circumferential flow angle on section A

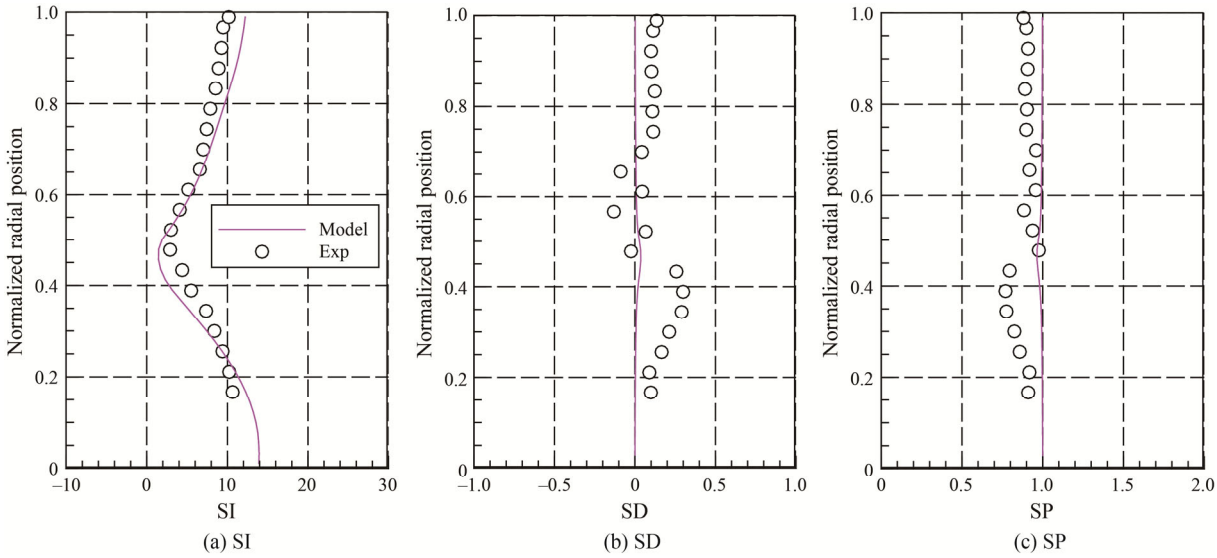

Fig. 9 Comparisons of radial distributions of swirl indexes

the SI decreases first and then increases along the radius, while the SD basically remains around 0 and the SP is always close to 1.

4.2 Transfer behavior of paired swirl in compressor

The flow characteristics of the two-stage compressor in the condition of the paired swirl distortion are obtained through the 3-D body force model. Table 3 presents the comparison between the simulated and experimental results of the overall characteristics for the studied operating point, which is in good agreement.

Figs. 10 and 11 compare the computed distributions of the absolute and relative circumferential flow angles at the rotor outlet of the first stage (i.e. the section B) with

the experimental results. It can be seen that the key flow features captured by the body force model are basically similar to the experimental results. Although the maximum region (red region) of the absolute flow angle calculated by the model is larger than that measured in the experiment, this can be narrowed by improving the deviation angle and loss model based on in-house empiricism and expertise. The results indicate that the blade force model effectively loads the turning effect of the blade row on the local flow under the swirl distortion. Therefore, it is believed that the body force model has sufficient potential to quantify the large-scale characteristics of the paired swirl distortion in the compressor.

Fig. 12 gives the contours of the absolute flow angle and dimensionless axial mass flux at the first stage inlet. The absolute flow angle at the rotor inlet of the first stage has great nonuniformity along the radial and circumferential directions. The value reaches the extreme value in the near end wall. The flow tends to enter axially in the middle of the blade. It indicates that the maximum swirl intensity of the twin swirl is near the end wall and the minimum is in the middle of the blade. Furthermore, it can be found that the direction of the absolute flow angle in the upper and lower near end wall at the same circumferential position is opposite, which is a typical feature of the paired swirl distortion [1]. Additionally, stronger suction effect of the rotor passages within a region of co-swirl on the upstream flow is obtained resulting in a larger inlet mass flux while the inlet mass flux of the blade passages within a region of counter-swirl is relatively small.

Fig. 13 reports the contours of the dimensionless total pressure and total temperature at the first stage outlet. The total pressure and total temperature distortion are observed during the transfer process of the paired swirl distortion in the first stage. It is generally known that the blade loading mainly depends on the inlet mass flux (axial velocity) and the swirl (tangential velocity). Comparing Fig. 12 with Fig. 13, we can find that the swirl of the first stage inlet plays a major role for the

Table 3 Overall characteristics of the studied operating point with paired swirl distortion

	Flow coefficient	Total-static pressure rise	Efficiency
Calculation	0.819	0.913	0.874
Experiment	0.792±0.003	0.903±0.004	0.876±0.006

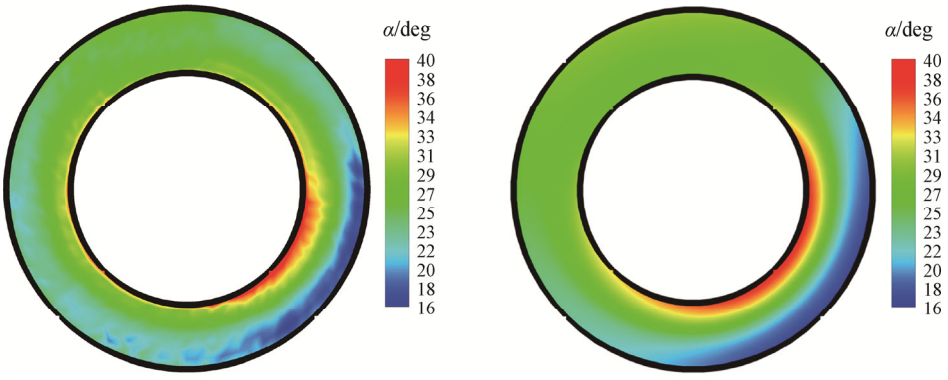

(a) Experimental results (b) Calculated results

Fig. 10 Distributions of absolute flow angle on section B

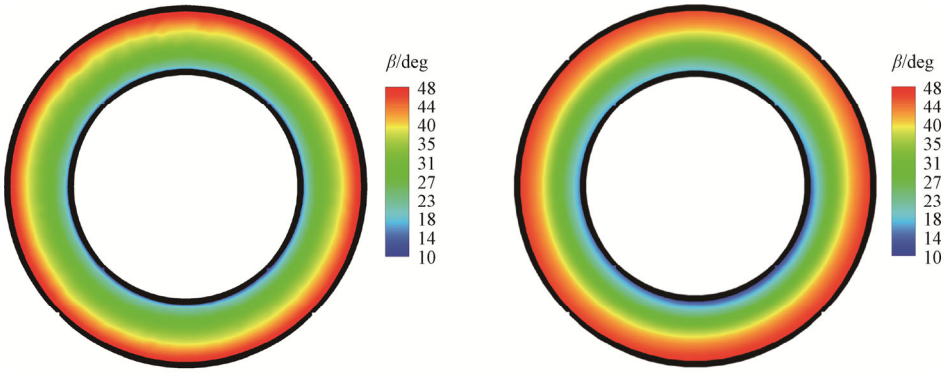

(a) Experimental results (b) Calculated results

Fig. 11 Distributions of relative flow angle on section B

variation of the rotor local operating condition. The upstream counter-swirl increases the amount of local work input to the flow by the rotor while the upstream co-swirl reduces the work input provided by the rotor.

Fig. 14 presents the contours of the absolute flow angle and the dimensionless mass flux at the second stage inlet. It can be seen that the swirl intensity is greatly reduced after the rectification of the first-stage stator and the flow direction at different positions, especially near the tip, is close to the axial direction. Hence, the blade loading of the second stage is mainly determined by the inlet mass flux, which is different from the first stage. Moreover, the nonuniformity of the mass flux induced by the swirl distortion at the compressor inlet still exists.

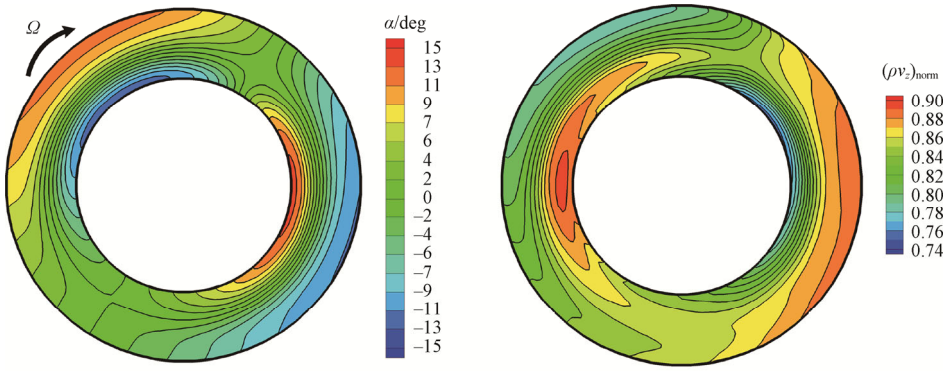

(a) Absolute flow angle (b) Dimensionless mass flux

Fig. 12 Contours of absolute flow angle and dimensionless mass flux at first stage inlet

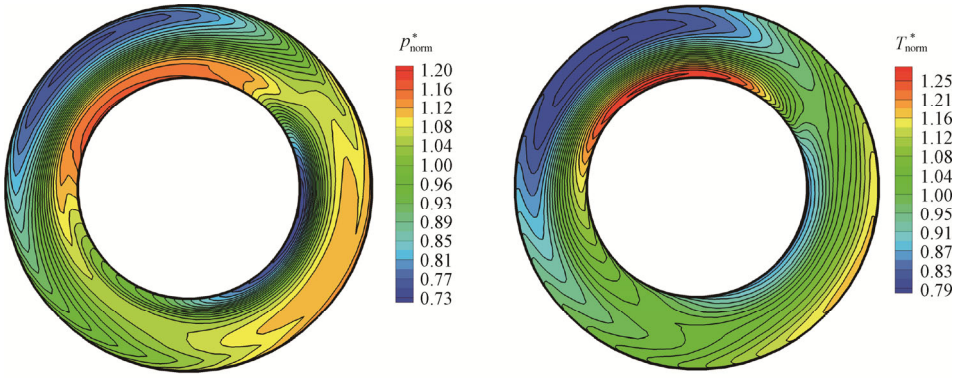

(a) Total pressure contour (b) Total temperature contour

Fig. 13 Contours of dimensionless total pressure and total temperature at first stage outlet

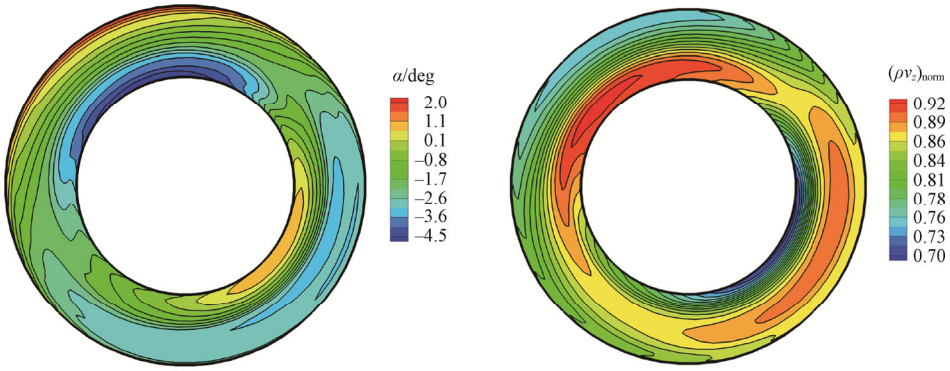

(a) Absolute flow angle (b) Dimensionless mass flux

Fig. 14 Contours of absolute flow angle and dimensionless mass flux at second stage inlet

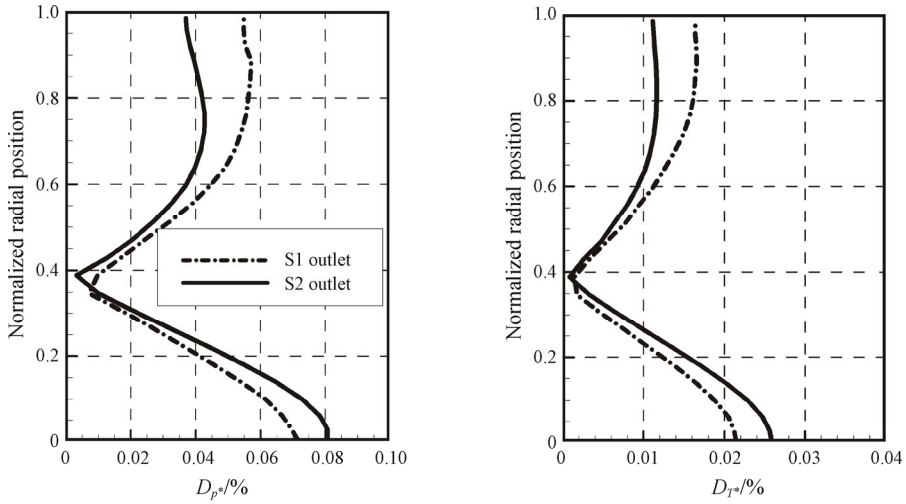

(a) Total pressure distortion intensity (b) Total temperature distortion intensity

Fig. 15 Radial distributions of distortion intensity at each stage outlet

Fig. 15 displays the radial distributions of the total pressure and total temperature distortion intensity at each stage outlet. The terms D_{p^*} and D_{T^*} are defined as follows:

$$\begin{cases} D_{p^*} = \dfrac{\overline{p^*} - \overline{p^*_{\text{low}}}}{\overline{p^*}} \\ D_{T^*} = \dfrac{\overline{T^*_{\text{high}}} - \overline{T^*}}{\overline{T^*}} \end{cases} \tag{21}$$

where $\overline{p^*}$ and $\overline{T^*}$ are the circumferential average total pressure and total temperature on a certain radius, respectively. The term $\overline{p^*_{\text{low}}}$ represents the average total pressure of the region below the value of $\overline{p^*}$. The term $\overline{T^*_{\text{high}}}$ is the average total temperature of the region above the value of $\overline{T^*}$. As can be found, different transfer features of the total pressure and total temperature distortion induced by the first stage are obtained at different heights of the second stage. Comparing Fig. 13 with Fig. 14, the high total pressure region near the tip of the second stage inlet has the larger inlet mass flow and thus the work capacity of the rotor passages in this region is reduced. By the contrast, the low total pressure region has the smaller mass flow and the work capacity of the rotor passages in the corresponding region is enhanced. Finally, the combined distortion is significantly attenuated near tip as it passes through the second stage. Although the distribution of the mass flow near the hub region of the second stage inlet is similar to that near the tip, the sensitiveness of the rotor work capacity to the variation of the inlet mass flow is decreased due to the lower rotor rim speed near hub. Besides, there is still about 4° of negative swirl in the high total pressure region near hub, which increases the work capacity of rotor passages in the region. Thus the distortion intensity is slightly enhanced at the hub of the second stage outlet. The above phenomenon reveals the complex 3-D characteristics of the interaction process between swirl distortion and multistage axial-flow compressors.

In order to further quantify the transfer process of swirl distortion in the two-stage compressor, Fig. 16 reveals the axial distributions of the swirl distortion intensity D_S at different span in the compressor. The term D_S, on the basis of Eq. (18), further includes the effect of the circumferential nonuniformity of the absolute flow angle as shown in Eq. (22).

$$D_S = \frac{\int_0^{360^\circ} \left|\alpha(\theta) - \bar{\alpha}\right| \mathrm{d}\theta}{360^\circ} \tag{22}$$

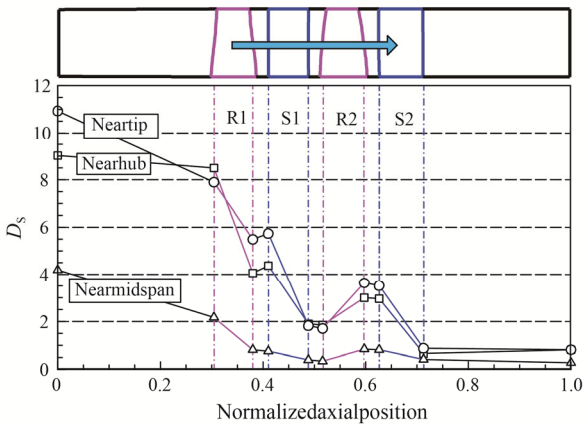

Fig. 16 Axial distributions of swirl distortion intensity at different span in compressor

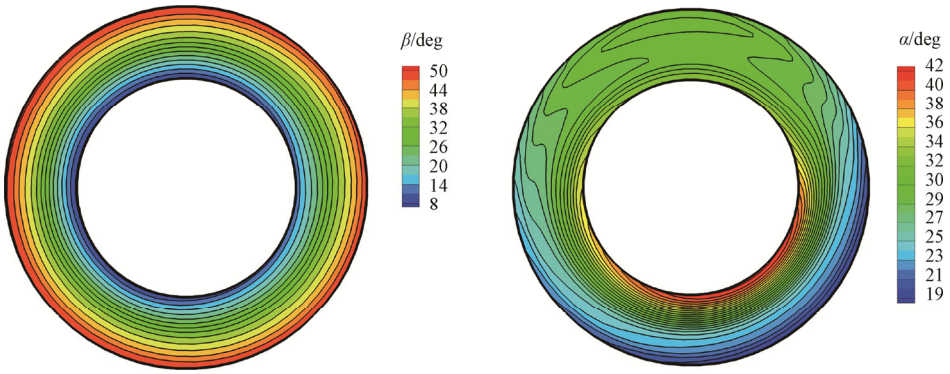

(a) Relative flow angle (b) Absolute flow angle

Fig. 17 Contours of flow angle at rotor outlet of second stage

where $\alpha(\theta)$ is the distribution of the absolute flow angle along the circumference at a certain blade height and $\bar{\alpha}$ is the average value of the absolute flow angle along the circumference at that blade height.

It can be observed that the variations of the swirl distortion intensity at different span along the axial flow of the compressor are basically consistent. The mixing flow in the circumferential direction occurs upstream the compressor resulting in the decrease of the swirl distortion intensity. The intensity decreases when passing through the passages of the first-stage rotor and stator. After passing through the second-stage rotor, the intensity slightly increases. Ultimately the intensity almost reduces to 0 through the rectification of the second-stage stator. The reason for the enhancement of the intensity in the passages of the second-stage rotor is that the flow at the second stage inlet basically tends to enter axially while the axial velocity is still not uniform (see Fig. 14). It can be seen from Fig. 17(a) that the distribution of the relative flow angle β is relatively uniform after the second-stage rotor. The quantitative relationship between the relative and absolute flow angles is shown in Eq. (23). The nonuniform distribution of the axial velocity results in the increase of the distortion of the absolute flow angle, as displayed in Fig. 17(b).

$$\tan\beta = \frac{U - v_\theta}{v_z} = \frac{U}{v_z} - \tan\alpha \tag{23}$$

5. Conclusions

Following the idea of the body force method, a mathematical model is developed to efficiently simulate the vane-based swirl distortion generator through distributed source terms. The internal flow characteristics of a two-stage low-speed axial compressor with paired swirl distortion are analyzed by combining the established mathematical model with a previously-developed 3-D body force model. The typical flow structure of the paired swirl generated by the swirl generator and the main distributions of the flow angle at the rotor outlet of the first stage captured by the model agree well with experimental results. Only a few hours are required during the whole calculation. It reveals that the model can quickly and reasonably reproduce the key flow feature of the paired swirl and quantify the large-scale characteristics of the paired swirl distortion in the flow process of the compressor.

The numerical results show that the intensity of the swirl distortion can be greatly reduced after passing through the whole compressor due to the rectifying effect of the stator row. However, the swirl induces the nonuniform distribution of the axial velocity as well as total pressure and total temperature distortion by leading to the variation of local blade loading of the first-stage rotor. Through the action of the second stage, the induced total pressure and total temperature distortion is significantly attenuated near tip and slightly enhanced near hub.

In general, the present study has constructed a satisfactory numerical strategy for compressor designers to reliably evaluate the 3-D flow behavior of multistage axial compressors in response to complex swirl distortion with acceptable calculation expense, which has certain engineering application value.

Acknowledgements

The research was funded by National Science and Technology Major Project (Grant 2017-II-0004-0017).

References

[1] Society of Automotive Engineers, A methodology for assessing inlet swirl distortion. Aerospace Information Report No. AIR 5686, 2010.

[2] Genssler H.P., Meyer W., Fottner L., Development of intake swirl generators for turbo jet engine testing. Technical report, DTIC Document, 1987.

[3] Sheoran Y., Bouldin B., A versatile design of a controlled swirl distortion generator for testing gas turbine engines.

ASME Turbo Expo, 2008, Paper No. GT2008-50657, pp. 81–92.

[4] Sheoran Y., Bouldin B., Krishnan P.M., Advancements in the design of an adaptable swirl distortion generator for testing gas turbine engines. ASME Turbo Expo, 2009, Paper No. GT2009-59146, pp. 23–32.

[5] Bouldin B., Sheoran Y., Inlet flow angularity descriptors proposed for use with gas turbine engines. World Aviation Congress and Exposition, 2002, SAE2002-01-2919.

[6] Hoopes K.M., O'Brien W.F., The StreamVane method: a new way to generate swirl distortion for jet engine research. 49th AIAA/ASME/SAE/ASEE Joint Propulsion Conference, 2013, AIAA Paper No. 2013-3665.

[7] Guimarães T., Lowe K.T., O'Brien W.F., StreamVane turbofan inlet swirl distortion generator: mean flow and turbulence structure. Journal of Propulsion and Power, 2018, 34(2): 340–353.

[8] Frohnapfel D.J., Lowe K.T., O'Brien W.F., Experimental quantification of fan rotor effects on inlet swirl using swirl distortion descriptors. Journal of Engineering for Gas Turbines and Power, 2018, 140(8): 082603.

[9] Dong X., Sun D., Li F., et al., Effects of stall precursor-suppressed casing treatment on a low-speed compressor with swirl distortion. Journal of Fluids Engineering, 2018, 140(9): 091101.

[10] Pardo A.C., Mehdi A., Pachidis V., et al., Numerical study of the effect of multiple tightly-wound vortices on a transonic fan stage performance. ASME Turbo Expo, 2014, Paper No. GT2014-26481.

[11] Yao J., Gorrell S.E., Wadia A.R., A time-accurate CFD analysis of inlet distortion induced swirl in multistage fans. 3rd AIAA/ASME/SAE/ASEE Joint Propulsion Conference and Exhibit, 2007, AIAA Paper No. 2007-5059.

[12] Fidalgo V.J., Hall C.A., Colin Y., A study of fan-distortion interaction within the NASA rotor 67 transonic stage. Journal of Turbomachinery, 2012, 134(9): 051011.

[13] Cousins W.T., Davis M.W., Evaluating complex inlet distortion with a parallel compressor model Part 1—Concepts, theory, extensions, and limitations. ASME Turbo Expo, 2011, Paper No. GT2011-45067, pp. 1–12.

[14] Davis M.W., Cousins W.T., Evaluating complex inlet distortion with a parallel compressor model Part 2—Applications to complex patterns. ASME Turbo Expo, 2011, Paper No. GT2011-45068, pp. 13–23.

[15] Hale A., O'Brien W., A three-dimensional turbine engine analysis compressor code (TEACC) for steady state inlet distortion. Journal of Turbomachinery, 1998, 120: 422–430.

[16] Hale A., Davis M., Sirbaugh J., A numerical simulation capability for analysis of aircraft inlet-engine compatibility. ASME Turbo Expo, 2004, Paper No. GT2004-53473, pp. 127–137.

[17] Gong Y., A computational model for rotating stall and inlet distortions in multistage compressors. Cambridge: Massachusetts Institute of Technology, 1998.

[18] Chima R.V., A three-dimensional unsteady CFD model of compressor stability. ASME Turbo Expo, 2006, Paper No. GT2006-90040, pp. 1157–1168.

[19] Sirovich L., Initial and boundary value problems in dissipative gas dynamics. Physics of Fluids, 1967, 10(1): 24–34.

[20] Guo J., Hu J., A three-dimensional computational model for inlet distortion in fan and compressor. Proc IMechE, Part A: Journal of Power and Energy, 2018, 232: 144–156.

[21] Marble F.E., Three-dimensional flow in turbomachines, aerodynamics of turbines and compressors. Princeton: Princeton University Press, 1964.

[22] Carter A.D.S., Hughes H.P., A theoretical investigation of the effect of profile shape on the performance of aerofoils in cascade. Aeronautical Research Council Reports and Memoranda 1946, pp. No. 2384.

[23] Lieblein S., Aerodynamic design of axial-flow compressors. VI-experimental flow in two-dimensional cascades. NACA Research Memorandums, Report No. NACA-RM-E55K01a, 1965.

[24] Roberts W.B., Serovy G.K., Sandercock D.M., Design point variation of three-dimensional loss and deviation for axial compressor middle stages. Journal of Turbomachinery, 1988, 110(4): 426–433.

[25] Lakshminarayana B., Methods of predicting the tip clearance effects in axial flow turbomachinery. Journal of Basic Engineering, 1970, 92(3): 467–482.

[26] Howell A.R., Fluid dynamics of axial compressors. Proceedings of the Institution of Mechanical Engineers, 1945, 153(1): 441–452.

[27] Banjac M., Petrovic M.V., Wiedermann A., Secondary flows, endwall effects, and stall detection in axial compressor design. Journal of Turbomachinery, 2015, 137(5): 051004.

[28] Jameson A., Schimidt W., Turkel E., Numerical solutions of the Euler equations by finite volume methods with Runge-Kutta time stepping schemes. 14th Fluid and Plasma Dynamics Conference, 1981, AIAA Paper No. 81-1259.

[29] Edwards J.R., A low-diffusion flux-splitting scheme for Navier-Stokes calculations. Computers & Fluids, 1997, 26(6): 635–659.

[30] Van L.B., Upwind-difference methods for aerodynamics problems governed by the Euler equations of gas dynamics. Lectures in Applied Mathematics. 1985, 22: 327–336.

[31] Gallimore S.J., Spanwise mixing in multistage axial flow compressors: Part II, Throughflow calculations including mixing. Journal of Turbomachinery, 1986, 108(1): 10–16.